ELSEVIER

Contents lists available at ScienceDirect

Construction and Building Materials

journal homepage: www.elsevier.com/locate/conbuildmat





Engineering properties and pore structure of lightweight aggregates produced from off-spec fly ash

Mohammad Balapour ^{a,*}, Thiha Thway ^b, Newell Moser ^c, Edward J. Garboczi ^c, Y. Grace Hsuan ^a, Yaghoob Farnam ^a

- a Drexel University, Department of Civil, Architectural and Environmental Engineering, 3141 Chestnut Street, Philadelphia, PA 19104, USA
- b Drexel University, Department of Chemical Engineering, 3141 Chestnut Street, Philadelphia, PA 19104, USA
- ^c National Institute of Standards and Technology, Applied Chemicals and Materials Division, 325 Broadway, Boulder, CO 80305, USA

ARTICLE INFO

Keywords: Waste fly ash Lightweight aggregate Sorption properties Pore size distribution X-ray computed tomography

ABSTRACT

This study characterizes the engineering properties of lightweight aggregate (LWA) manufactured from low calcium (F-FA) and high calcium (C-FA) waste fly ash that were designed using a previously-developed thermodynamics-guided process. LWA properties that were characterized include specific gravity, vacuum water absorption, water absorption over time, water desorption, porosity, pore size distribution, and permeability. The LWA studied had a low oven dry specific gravity ranging from 1.22 to 1.45. The vacuum absorption and total open porosity of F-FA LWA decreased as the fluxing agent (NaOH) concentration increased while the values for C-FA LWA varied with increasing amounts of fluxing agent. All LWA passed the ASTM C1761 water absorption/ desorption requirements for application to the internal curing of concrete. X-ray computed tomography (XCT) and dynamic vapor sorption analyzer (DVSA) techniques were used to characterize the LWA pore structure. It was found that for F-FA LWA the normalized porosity, counting only pores smaller than 50 nm (gelpores + mesopores), ranged from 4 % to 11.5 %, while for C-FA LWA, this same pore size range had porosity ranging from 1.7 % to 2.8 %. Pore size distribution measurements of F-FA LWA using XCT showed that the pores became larger and the predicted permeability coefficient increased as the fluxing agent concentration increased. For C-FA LWA, the predicted permeability increased with increasing NaOH concentration. Since the pore size distribution had greater variability and did not follow a specific increasing trend, the increase in C-FA permeability could only be due to an increase in pore connectivity.

1. Introduction

Waste coal combustion ash (W-CCA) is one of the largest-volume industrial solid waste materials historically produced in the US. In 2019, 78 million tonnes of coal combustion products were produced, of which only 52 % was recycled and the rest moved to surface impoundments or landfills [1]. Fig. 1 shows the total CCA production and recycled fraction over the last 20 years [1]. As can be seen, although the recycling rate has slightly increased over the last 20 years, it is estimated that 1.45 billion tonnes of W-CCA have accumulated in landfills during this same 20-year period. Averaged over the last 20 years, the percentage of W-CCA recycling has been only 45 %. Keeping accumulated W-CCA in surface impoundments or landfills has negative impacts such as pollution of waterways, groundwater, drinking water, which subsequently can damage human health. Two relatively recent examples of W-CCA damage are the catastrophic Kingston Fossil Plant coal fly ash

slurry spill (Tennessee, 2008) [2] and the Dan River coal ash spill (North Carolina, 2014) [3], where not only long-term environmental damage was caused to the waterways, but human health was compromised. Increasing the W-CCA recycling rate through developing sustainable uses for this material will promote diversion of material away from landfills and surface impoundments.

Fly ash constitutes approximately 35 % of the annual production of W-CCA, of which only 55 % to 60 % is recycled [1]. The main application of recycled fly ash is in concrete as a pozzolanic material [4]. Unrecycled fly ash (so called off-spec fly ash) cannot be directly used in concrete because it does not meet the ASTM C618 [5] or AASHTO M 295 [6] requirements: (i) Loss on Ignition (LOI) of less than 5 % (by mass), (ii) providing a strength index of greater than 75 % through pozzolanic reaction with cement, and (iii) sulfur trioxide (SO₃) content of less than 3 % (by mass). However, unrecycled fly ash can be used as a raw material for the production of construction lightweight aggregate (LWA).

^{*} Corresponding author.

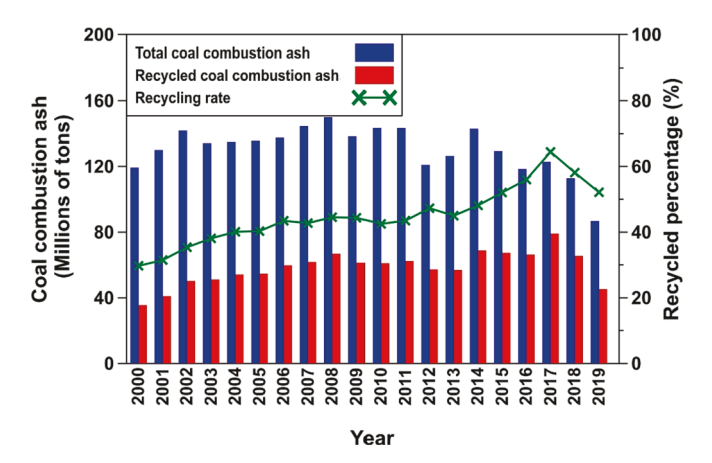


Fig. 1. Production and recycled percentage of coal combustion ash during the past 20 years [1].

Natural resources such as clay, shale, and slate are the raw materials commonly used for the production of traditional construction LWA [7]. The use of waste fly ash for LWA production can reduce the use of these natural resources.

Accessibility of construction LWA for applications such as light-weight concrete, internal curing of concrete, and lightweight concrete masonry blocks is challenging within some states of the United States due to the absence of local construction LWA manufacturers (e.g., PA, NJ, and DE) [8]. For this reason, concrete manufacturers are forced to import construction LWA from far distances, which results in a high final cost due to the added transportation cost. Using waste fly ash, which is an abundant raw material in many states, can increase the local accessibility of construction LWA for concrete producers.

Many available studies in the literature focus on the production of LWA from in-spec fly ash (i.e., the fly ash that can be directly used in concrete) and use a trial-and-error method for their development [9–12]. Balapour et al. [13] and Billen et al. [14,15] previously developed a thermodynamics-based approach to convert W-CCA, including bottom ash and fly ash, into LWA and quantified the three required conditions for the high temperature production of LWA: (i) partial formation of a liquid phase, (ii) appropriate viscosity for solid–liquid phase, and (iii) formation of gaseous products that are entrapped by the liquid phase to create a porous LWA structure. Based on these conditions, the appropriate ranges of temperature and viscosity to successfully produce porous LWA were identified [13]. The objective of this study is to evaluate the engineering properties of W-CCA LWA that were systematically produced based on the thermodynamics-based methodology developed previously [13,14,16].

LWA engineering properties relevant to applications such as structural lightweight concrete [17] and concrete internal curing [16,18] were characterized. Specific gravity and open porosity were measured to ensure the successful formation of LWA after the sintering process. Vacuum water absorption was performed to quantify the maximum absorption capacity of LWA. Time-dependent water absorption was assessed to obtain the practical absorption capacity of the LWA and determine whether the LWA is an appropriate candidate for concrete applications. Water desorption behavior of the LWA was evaluated using a dynamic vapor sorption analyzer (DVSA) to determine the capability of LWA in releasing absorbed water to the cement paste matrix during hydration and to characterize the pore size distribution of the LWA in the range of pores smaller than 50 nm, according to the Kelvin-Young-Laplace equation [19]. X-ray computed tomography was used to characterize porosity, pore size distribution, and predicted permeability of the LWA for pores larger than 19 µm. Table 1 summarizes the experimental program for this study.

Table 1Experimental program.

Experiment	Purpose
Buoyancy	To assess the oven dry, saturated surface dry and apparent specific gravity of the LWA
Vacuum absorption	To evaluate the maximum water absorption capacity and total open porosity of the LWA
Time dependent absorption	To assess the water absorption of LWA over time
DVSA	To evaluate the water desorption behavior of LWA and characterize its pore structure at pore range smaller than 50 nm
XCT	To characterize porosity, pore size distribution, and permeability of LWA at pore sizes greater than 19 μm

2. Materials and sample preparation

Two types of off-spec fly ash were used in this study, which based on their chemical composition according to ASTM C618 [5] can be categorized as: (i) low calcium class F fly ash (F-FA) and high calcium class C fly ash (C-FA). Table 2 shows the chemical oxide composition of the off-spec fly ashes as obtained through X-ray fluorescence (XRF). One of the most important requirements of ASTM C618 for fly ash is a LOI of less than 6 % (by mass). In addition, based on AASHTO M 295, the LOI limit for fly ash in more than thirty-nine states must be less than 5 %. Accordingly, fly ashes used in this study can be classified as off-spec fly ash owing to a high LOI content (see Table 2).

Quantitative X-ray diffraction (QXRD) analysis was performed across the range of 5° to 80° 2 θ with a 0.02° step size on both fly ashes to quantify their amorphous content and crystalline phases. 20 % rutile (TiO₂) was used as an internal standard for the purpose of quantification [20]. Use of rutile might result in underestimation of amorphous phase content. This effect was not further investigated as it was out of the scope of this study. Table 3 shows the crystalline phases and amorphous content of the ashes, which indicates that a significant portion of the ashes is composed of an amorphous phase.

The manufacturing of FA-LWA includes four main steps: drying, pelletization, curing, and sintering. In the first step, the ashes were dried in an oven at 110 $^{\circ}\text{C} \pm 5$ $^{\circ}\text{C}$ for 24 h to remove their moisture. In the second step, pelletization, the dried ash was mixed with NaOH aqueous solution with molarities of 0 mol/L (i.e., deionized (DI) water), 2.5 M, 5 M, 7.5 M, 10 M, or 12.5 M with a liquid to solid (L/S) mass ratio of 0.2. These concentrations led to mass concentrations (i.e., mass of solid NaOH per mass of solid fly ash) of 0 %, 2 %, 4 %, 6 %, 8 %, and 10 %. The ash and aqueous NaOH (or deionized water) were mixed thoroughly to achieve a homogenous mixture. Afterwards, a plastic mold of 16 mm diameter was used to pelletize each mixture into a spherical shape. An L/S ratio of 0.2 was found to be the minimum ratio needed for the

Table 2 Chemical oxides of off-spec fly ash based upon a single measurement.

Chemical composition	Sample Name	
(% by mass)	F-FA	C-FA
SiO_2	49.5	38.2
Al_2O_3	23.8	18.8
Fe ₂ O ₃	15.4	10.9
SO_3	0.7	3.6
CaO	3.2	18.8
za ₂ O	0.4	1.1
MgO	1.6	3.6
K ₂ O	2.3	1.0
P_2O_5	_	0.7
TiO ₂	-	1.3
Total	97.0	97.9
LOI	5.3	8.5
Unburnt Carbon	2.3	7.0
Initial moisture content	0.4	1.2

Table 3The crystalline phases content of raw fly ashes (% by mass) based upon a single measurement.

Phase name	Sample name	
	F-FA	C-FA
Quartz	7.0	5.9
Mullite	10.7	3.5
Hematite	4.5	1.0
Anhydrite	1.9	3.0
Calcium aluminoferrite	0	1.6
Amorphous	75.9	84.9

successful formation of spherical fresh pellets. In step three, the pellets were cured in an environmental chamber at 40 $^{\circ}$ C and 30 $^{\circ}$ C relative humidity (RH) for 24 h. In the final step, the fresh aggregates (i.e., the cured pellets) were sintered at 1160 $^{\circ}$ C for 4 min to produce FA-LWA. Samples are designated as XX-YY%, where XX shows the type of materials (i.e., either F-FA or C-FA), while YY represents the NaOH concentration.

3. Testing methods

3.1. Specific gravity measurement

For each type of LWA with different NaOH concentrations, three replicates were randomly selected to perform the specific gravity test. The specific gravity of the aggregates was obtained by measuring their oven dry (OD), saturated surface dry (SSD), and apparent specific gravity in accordance with the ASTM C127 [21] buoyancy method. The vacuum absorption capacity was measured to investigate the maximum possible absorption capacity of the aggregates. The LWA was dried in an oven at 100 $^{\circ}\text{C} \pm 5 \,^{\circ}\text{C}$ for a minimum of 24 h to measure OD mass. About 1000 mL of deionized water was de-aerated in the vacuum pump for 1 h to remove the gas inside the water. The pump was then turned off and the deionized water container was removed from the chamber of the vacuum pump and covered with a lid for later procedures. The ovendried LWA were de-aerated in a vacuum pump at a pressure of 1.33 kPa \pm 0.33 kPa for 3 h to remove gas in the pores. After 3 h under vacuum conditions, the previously de-aerated deionized water was introduced to the LWA. The process lasted for an additional 1 h until the LWA were fully submerged in the water. The vacuum pump was then turned off, and the beaker was taken out of the chamber and kept in atmospheric conditions for 24 h. After vacuum saturation, the surface water of the aggregates was removed using an absorbent cloth and the SSD mass was recorded. After determining the SSD mass, the LWA was immediately placed into the buoyancy container filled with deionized water, and the apparent mass in the water was recorded at room temperature.

3.2. Absorption over time

For each type of LWA with different NaOH concentrations, three replicates were randomly selected to perform the water absorption test and measure the OD LWA water absorption property as a function of time. The LWA were dried in an oven at $110\,^{\circ}\text{C} \pm 5\,^{\circ}\text{C}$ for 24 h to remove the moisture inside the samples and the OD mass was measured. Next, the samples were placed in a container filled with tap water to fully cover the LWA samples. Then, at specific intervals, the samples were taken out of the container and their surface water was dried using an absorbent cloth to measure the SSD weight. Before each measurement, the container was carefully shaken to remove any potential entrapped air bubbles. The measurements were done at 30 min, 1 h, 2 h, 3 h, 4 h, 5 h, 6 h, 24 h, 36 h, 48 h and 72 h after the first contact of LWA with water.

3.3. Dynamic vapor sorption analyzer (DVSA)

The desorption/absorption behavior and nano/micropores of the LWA were characterized using a DVSA. A disk of 1 mm thickness was cut from the middle section of the lightweight aggregate using a diamond saw. The disk was broken into small pieces and soaked in water for 24 h. A piece with a mass of about 60 mg was used for testing in the DVSA instrument. The SSD sample was placed in a quartz pan at a constant temperature of 23 °C for both the desorption and absorption cycle. The RH was initially set to 97.5 % and decreased in increments of 1.5 % down to 96 %, then down to 90 % in increments of 2 %, then down to 80 $\,$ % in increments of 5 %, and finally decreased all the way to 0 % in increments of 10 %. After each increment, the RH was kept constant for either 96 h or, if the mass change was less than 0.001 mg over 15 min, then the instrument proceeded to the next RH value. This procedure was applied in reverse to increase the RH to 97.5 % for the absorption cycle. Due to the long duration of DVSA testing, only three NaOH concentrations (2 %, 6 %, and 10 %) for both F-FA and C-FA were selected for testing.

3.4. X-ray computed tomography (XCT)

A Zeiss Versa XRM 500^1 was used to perform XCT and evaluate the LWA pore structure. The X-ray tube was set for a voltage of 120 kV and a current of $83 \mu A$. The tube, specimen, and detector were arranged to give a reconstructed voxel size of about $19 \mu m$. The exposure time per step for a rotation of 360° was approximately 0.45 s. 2D projections of the LWA were collected and using the software supplied with the Zeiss Versa XRM 500, tomographic reconstruction was performed to reconstruct a 3D image, which was subsequently saved a stack of approximately 1000 2D cross-sectional slices each having thickness equal to the voxel size. The visualization and calculations presented in this paper were performed using Dragonfly Software [22].

In order to calculate the porosity of the LWA for each dataset, a cubic volume of interest (VOI) with a size of 7.5 mm \times 7.5 mm \times 7.5 mm was extracted from the center of each 3D XCT image. Different segmentation methods were tested (including Otsu [23], maximum entropy [24], and Bernsen [25]) and it was found that K-means ++ [26,27] clustering could yield the best performance in capturing the pore space in the images based upon visual comparison. K-means clustering segments all the pixels of an image into k clusters [28]. In this method, first (i) the centroids of the clusters are initialized, next (ii) for each pixel of the image the Euclidean distance to the center is calculated, then (iii) based on the obtained distance, the nearest pixels are assigned to a cluster, after that (iv) based on the assigned pixels new centers will be calculated, and finally (v) the process is repeated until it satisfies a tolerance value. K-means clustering is generally affected by the selection of K centroids at the first step. K-means ++ is an improved form of the basic K-means algorithm, where the only difference is in the selection of initial centroids [29]. In this method, (i) the first centroid is selected randomly, next (ii) the distance of each data point is calculated from the previously chosen centroid, then (iii) the next centroid is selected from the data points such that the probability of choosing that point as centroid is directly proportional to its distance from the nearest, previously chosen centroid, and finally (iv) steps (ii) and (iii) are repeated until K centroids are selected. It was found that using six clusters with eight iterations could most reasonably identify the pore space in the LWA. The high number of clusters was due to the close intensity of some portions of the solid and pore phases. The two first clusters were combined to form the

Certain commercial equipment, software and/or materials are identified in this paper in order to adequately specify the experimental procedure. In no case does such identification imply recommendation or endorsement by the National Institute of Standards and Technology, nor does it imply that the equipment and/or materials used are necessarily the best available for the purpose.

pore space and the rest of the clusters were the solid phase. Previously it has shown that pore-solid segmentation in image processing is one of the steps that can contribute to the uncertainty in quantitative analysis. However, uncertainty quantification was beyond the scope of this study [30]. Due to resolution limitation many of the micropores (specifically those smaller than 3 to 5 times the voxel size) could not be captured by the XCT [31], which could possibly result in errors in the calculated final porosity and predicted permeability. Fig. 2 shows an example raw and segmented image of C-FA 6 % LWA.

A plugin of Dragonfly software called OpenPNM¹ [32] was used for the extraction of pore network of the LWA from the segmented poresolid phase. The plugin uses an algorithm referred to as SNOW (subnetwork of the over-segmented watershed) [33], which is based on marker-based segmentation for the extraction of pores. This method consists of five steps. In the first step, the distance map of pore space in the binary image is obtained and smoothened using a Gaussian blur filter. In the second step, the peaks are identified in the distance map using a maximum filter with a spherical structuring element of radius R. A spherical structuring element with radius of 4 was used in this study [33]. In the third step, any extraneous peaks in the previous step is trimmed, which is the key to avoiding over-segmentation. A detailed description of this method can be found elsewhere [32–34]. In step four, the image is segmented into pore regions using a marker-based watershed segmentation method, where the corrected maxima identified in the previous step are used as the markers. Finally, the segmented image is used to obtain information about the pore and throat (channel) size in the network. In this study, for pore size distribution analysis pores were characterized by their equivalent diameter, which is the diameter of a sphere with equivalent volume to that of the identified pore. Fig. 3(a) shows the 3D reconstruction of the segmented solid phase in C-FA 6 % LWA, and Fig. 3(b) shows the extracted pore network model of the LWA in the VOI. Once the pore-throat network was extracted, the closed pores were excluded to generate a continuous medium of pore and throat to enable the calculation of the intrinsic permeability (or simply referred to as permeability in this paper) of the LWA.

At the pore-scale for incompressible fluid and a constant volume of a pore i, the sum of inflows and outflows must be equal, which can be written as the following equation:

$$\sum_{i=1}^{n} Q_{ij} = 0 \tag{1}$$

where n is the number of connections to and from pore i, and Q_{ij} is the volumetric flow from pore i to pore j, which is directly proportional to the pressure difference between the pores according to Equation 2):

$$Q_{ii} = g_{ii}(P_i - P_i) \tag{2}$$

The parameter g_{ij} is the conductance between pores i and j, and P_i and P_j are the fluid pressures in pores i and j. The conductance between pores is related to the throat diameter and length and fluid viscosity using Poiseuille's law according to Equation 3:

$$g_{ij} = \frac{\pi d_{ij}^4}{128\nu L} \tag{3}$$

where d_{ij} is the throat diameter between pores i and j, L is the throat length between pores i and j, and ν is the fluid viscosity.

Equations ((1)–(3))s can be combined to result in linear algebraic system for the unknown pore pressure at each pore. Considering the boundary conditions (pressure difference of 1 atm across the entire sample in each direction for calculating permeability at that direction), the equations can be solved to obtain the pore pressure at each pore. Knowing the pressure at each pore, the volumetric flow can be calculated. Finally, the permeability of the system is determined based on Darcy's law according to Equation (4) [35]:

$$K = \frac{Q\nu L}{4\Lambda P} \tag{4}$$

where Q is the total volume flow through the network, L is the length of the network, A is the cross-sectional area of the pore network perpendicular to the direction of flow, and ΔP is the boundary pressure difference (1 atm) in the \times , y, and z directions. Therefore, the associated permeability coefficient i.e., K_{xx} , K_{yy} , and K_{zz} (double subscript indicates flow in the same direction as the applied pressure gradient) can be obtained.

4. Results and discussion

4.1. LWA physical appearance

For each FA type, multiple replicates were produced to evaluate their physical appearance. The selected LWA were chosen to investigate how LWA physical appearance might change with respect to the FA type and NaOH concentration. High-quality digital camera images were taken

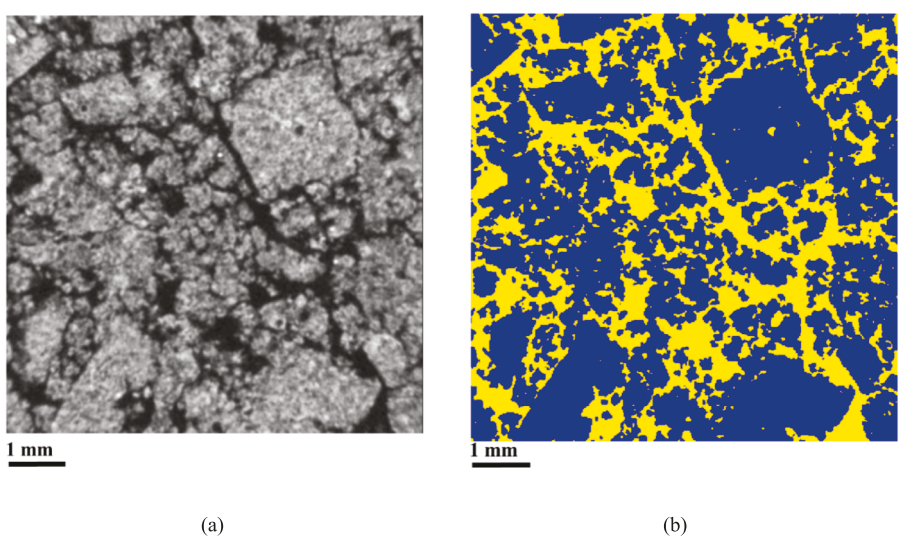


Fig. 2. C-FA 6 % LWA shown as an example of image segmentation; (a) raw image before segmentation and (b) segmented image into pore (yellow color) and solid (blue color) phase through k-means ++ clustering method. (For interpretation of the references to color in this figure legend, the reader is referred to the web version of this article.)

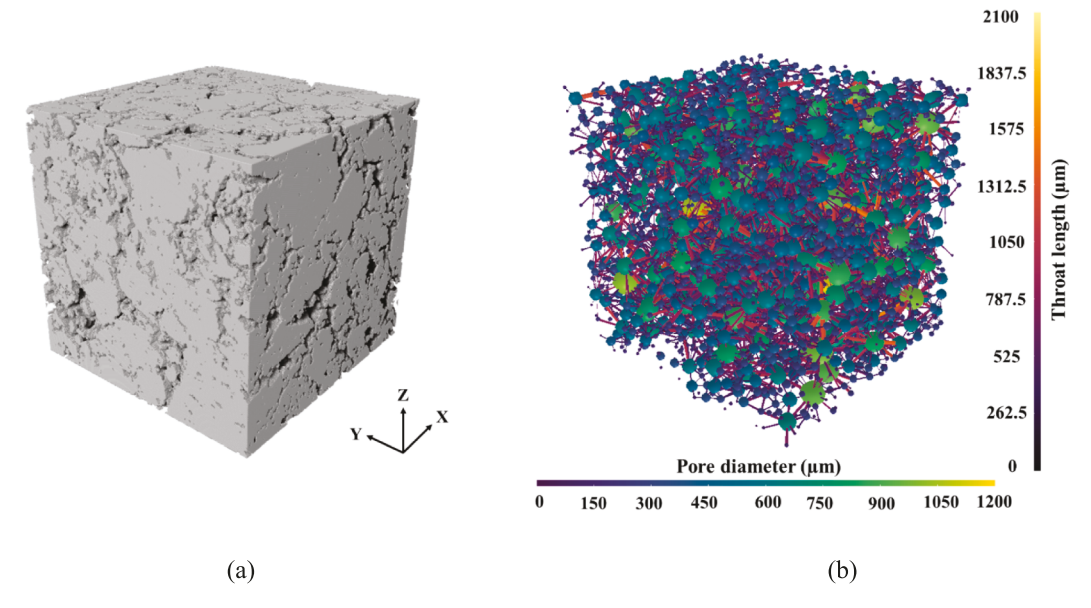


Fig. 3. C-FA 6% LWA shown as an example; (a) the VOI 3D reconstructed of segmented solid phase and (b) Pore Network Model of the LWA representing pores and throats.

from the front view of the LWA, where the distance between the LWA and camera was kept constant to achieve the same magnification for all images. Fig. 4 shows the front view physical appearance of the F-FA LWA samples. F-FA 0 % showed a red-brown color, while adding NaOH to the samples shifted the color toward dark brown. The addition of NaOH for F-FA 2 %, F-FA 4 %, and F-FA 6 % caused the occurrence of a subtle shiny surface, suggesting the formation of a liquid phase in the LWA during the sintering process. A local melting could be observed on the surface of F-FA 10 %, which probably suggests the presence of excessive NaOH concentration in the LWA.

Fig. 5 shows the front view physical appearance of the C-FA LWA samples. The addition of NaOH changed the color of C-FA LWA from yellow for C-FA 0 % to light brown for C-FA 10 %, except C-FA 8 %, which showed a dark brown color. As can be seen, C-FA 0 %, which was prepared with DI water without NaOH addition, had a smaller size compared to other C-FA LWA, which suggests shrinkage occurred after sintering. In addition, severe cracking could be observed on the surface

of C-FA 0 %, probably caused by a combination of lack of liquid phase formation and thermal shrinkage during cooling after sintering. The cracking was less observable on the surface for the C-FA LWA prepared with NaOH (i.e., C-FA 2 % to C-FA 10 %), which could be related to the formation of a liquid phase in the LWA by addition of NaOH. Balapour et al. showed that C-FA 0 % had $\sim\!15$ % liquid phase while C-FA 2 % had about 36 % liquid phase. Some local melting appeared on the surface of C-FA 8 % suggesting an NaOH concentration in excess of what was needed for sample preparation. It should be noted that all LWA had enough integrity and strength after sintering to be handled for further testing.

4.2. Specific gravity

Fig. 6 shows the oven dry (OD), saturated surface dry (SSD), and apparent (APP) specific gravity of F-FA LWA and C-FA LWA. Since the measured specific gravity for all the aggregates manufactured in this

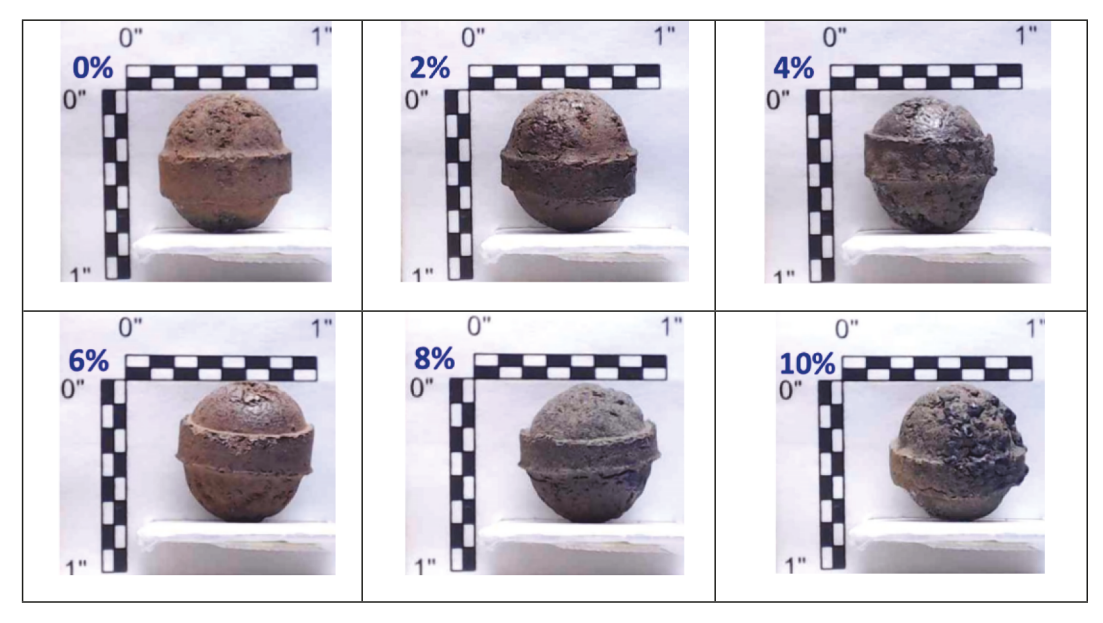


Fig. 4. The front view of F-FA LWA sintered at 1160 °C for 4 min; the upper left corner of each image shows the NaOH percentage.

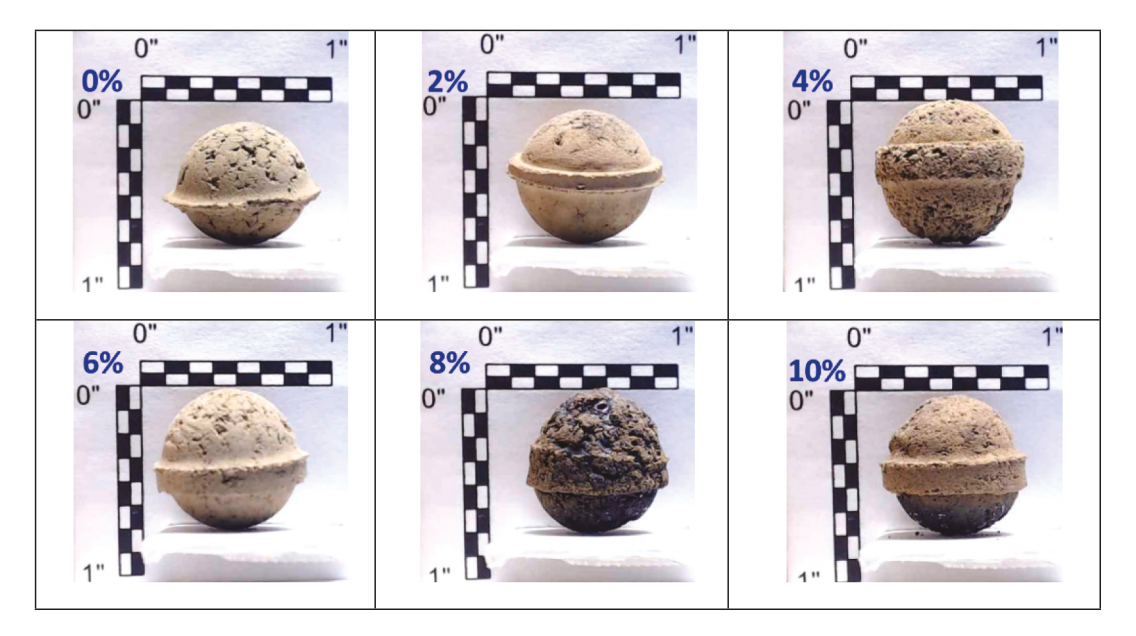


Fig. 5. The front view of C-FA LWA sintered at 1160 °C for 4 min; the upper left corner of each image shows the NaOH percentage.

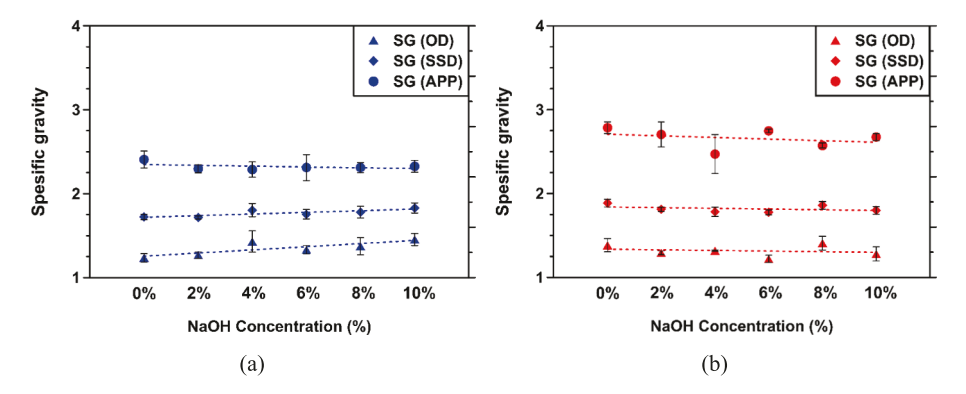


Fig. 6. Apparent (APP), oven dry (OD), and saturated surface dry (SSD) specific gravity of (a) F-FA LWA and (b) C-FA LWA (the error bars indicate \pm one standard deviation computed from three replicates).

study is less than 2, they can all be classified as LWA according to EN 13055 [36]. Fig. 6(a) shows that for F-FA LWA, increasing the NaOH concentration from 0 % to 10 % slightly increased the OD and SSD

specific gravity while the OD specific gravity changed from 1.24 to 1.45. This could be related to the increase in the solid weight of LWA due to the addition of higher solid NaOH concentration to the LWA. On the

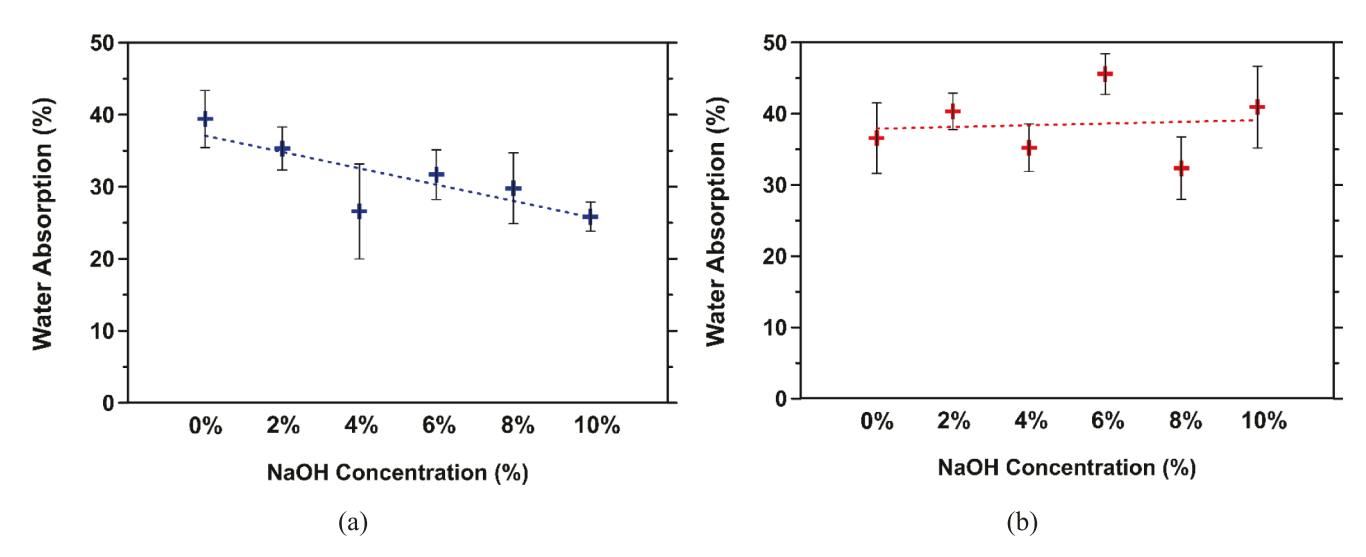


Fig. 7. Vacuum water absorption of (a) F-FA LWA and (b) C-FA LWA (the error bars indicate \pm one standard deviation computed from three replicates).

other hand, Fig. 6(b) shows that for C-FA LWA, the OD specific gravity had some variations at each NaOH concentration, and a clear trend could not be observed. The lowest specific gravity for C-FA LWA was that of C-FA 6 %, which was equal to 1.22. Balapour et al. [16] found a similar trend of specific gravity for LWA made from low and high calcium bottom ash. The APP specific gravity pertains to the solid portion of the LWA and the pore space among particles accessible to water is not considered. Comparing the apparent specific gravity of F-FA and C-FA LWA implies a higher net volume of solid particles for F-FA LWA, which has led to lower apparent specific gravity values for F-FA LWA.

4.3. Vacuum and time-dependent water absorption

Fig. 7 shows the vacuum water absorption for F-FA and C-FA LWA. Vacuum water absorption demonstrates the maximum possible absorption capacity for an LWA. As can be seen from Fig. 7(a), the vacuum absorption capacity of F-FA LWA decreased as the NaOH concentration increased. This could be related to the fact that higher NaOH concentration led to the development of closed porosity in F-FA LWA, which decreased vacuum absorption capacity. In a previous study, Balapour et al. [16] found a similar trend for LWA made from low calcium bottom ash. The highest average vacuum absorption capacity was 39.4 % for F-FA 0 %, and the lowest value was 25.8 % associated with F-FA 10 %. The vacuum absorption capacity for C-FA LWA, shown in Fig. 7b, displays a seemingly variable behavior, where the highest average vacuum absorption capacity was 45.6 % for C-FA 6 %. This variable behavior was previously observed for LWA made from high calcium bottom ash [16]. This observation implies the highly random nature of pore structure development in LWA made from high calcium coal ash, both fly ash and bottom ash.

Fig. 8 shows the water absorption of F-FA and C-FA LWA over a 72 h period. All the LWA had a 72 h water absorption of greater than 5 %, as required by ASTM C1761 [37] for a LWA to be used for internal curing of concrete. The first water absorption measurement was made 30 min after soaking the LWA in water. As can be seen for both types of LWA, more than 70 % of the 72 h water absorption occurred in the first 30 min. This observation demonstrates the highly connected pore structure of LWA with a high number of capillary pores that led to rapid and efficient water absorption.

For F-FA LWA (Fig. 8 (a)), the 72 h water absorption order was as follows: F-FA 0 % > F-FA 6 % > F-FA 8 % > F-FA 10 % > F-FA 2 % > F-FA 4 %. Comparing the water absorption for F-FA 0 % to other F-FA LWA

suggests that the addition of NaOH to the LWA decreased the absorption capacity of the LWA. The same behavior is also observed in C-FA LWA (Fig. 8(b)). The water absorption order of C-FA LWA was as follows: C-FA 0 % > C-FA 6 % > C-FA 10 % > F-FA 8 % > C-FA 2 % > C-FA 4 %. C-FA LWA showed a higher water absorption capacity compared to the respective F-FA LWA with the same NaOH concentration. This behavior could be related to a smaller number of closed pores available in the microstructure of C-FA LWA so that water absorption through the connected pores could be higher.

Fig. 9 shows a comparison between the vacuum and 72 h water absorption for F-FA and C-FA LWA. The vacuum water absorption shows the maximum possible water absorption for the LWA, whereas the 72 h water absorption is the value that is usually used in practice. The gray area shown on the figure demonstrates the amount of extra water absorbed by the LWA under vacuum compared to the 72 h water absorption. The extra amount of water could not be absorbed through capillary suction of the pores in the LWA during the 72 h period. In theory, if the LWA is soaked in water for an infinite amount of time, the time dependent absorption should approach the vacuum water absorption. On the other hand, differences between the vacuum and 72 h water absorption indicates that not all the pores could be filled with water during the 72 h period. This could be caused by the presence of trapped gas in the pores during water absorption, which can delay the absorption mechanism in the LWA [38]. For F-FA LWA, the gray area in Fig. 9, which is the difference between the 72 h and vacuum water absorption, got smaller at higher NaOH concentrations (F-FA 6 %, F-FA 8 %, and F-FA 10 %), meaning the vacuum and 72 h water absorption values were becoming closer in value. In contrast, the difference between vacuum absorption and 72 h absorption showed a variable behavior as a function of NaOH for C-FA LWA. The 72 h absorption of both F-FA and C-FA LWA showed that the addition of NaOH up to 4 % decreased the absorption but beyond this amount the absorption sharply increased and remained relatively constant from 6 % to 10 %. Ren et al. [39] observed the same trend for LWA prepared with fly ash, clay, and sodium carbonate as the fluxing agent. This trend could be related to the formation of liquid phase, which is promoted by the amount of NaOH in LWA. The liquid phase forms on the surface of LWA [13,16,40], which could potentially acts as a barrier for LWA water absorption. When the NaOH concentration passed 4 %, rearrangement of pores in the excessive liquid phase (formed by higher NaOH concentration) that had a lower viscosity enabled higher 72 h water absorption [13].

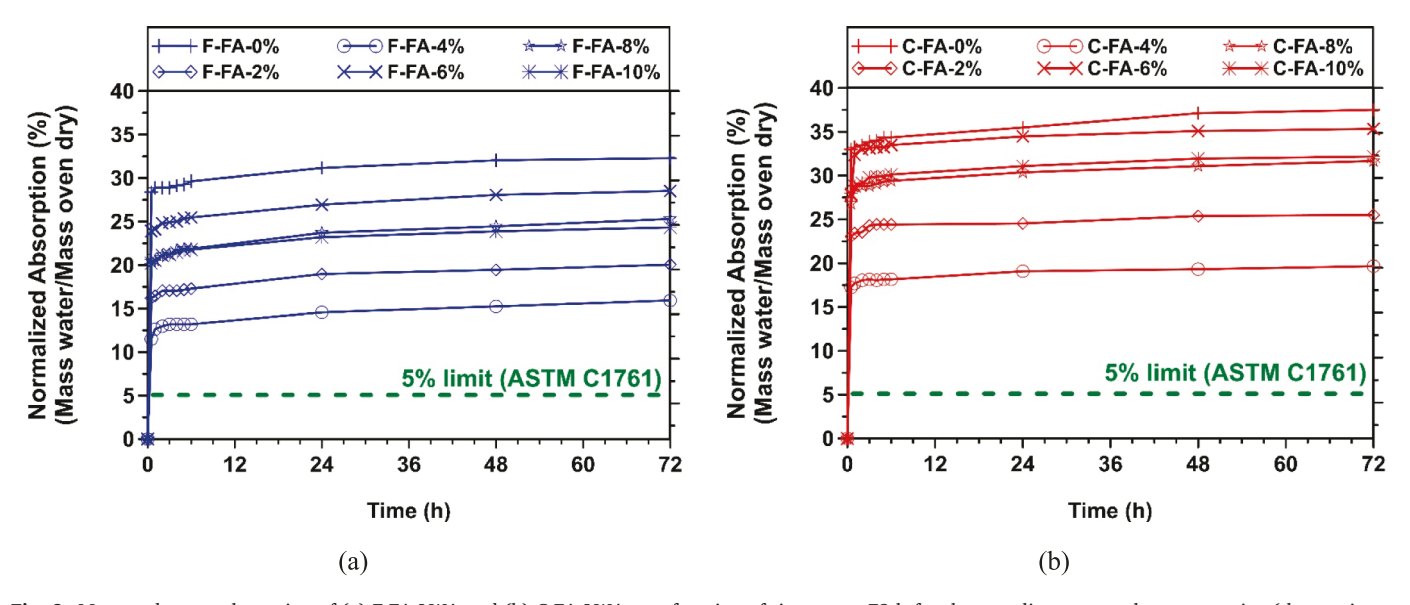


Fig. 8. Measured water absorption of (a) F-FA LWA and (b) C-FA LWA as a function of time up to 72 h for three replicates at each concentration; (the maximum standard deviation for three replicates was determined to be 9 %).

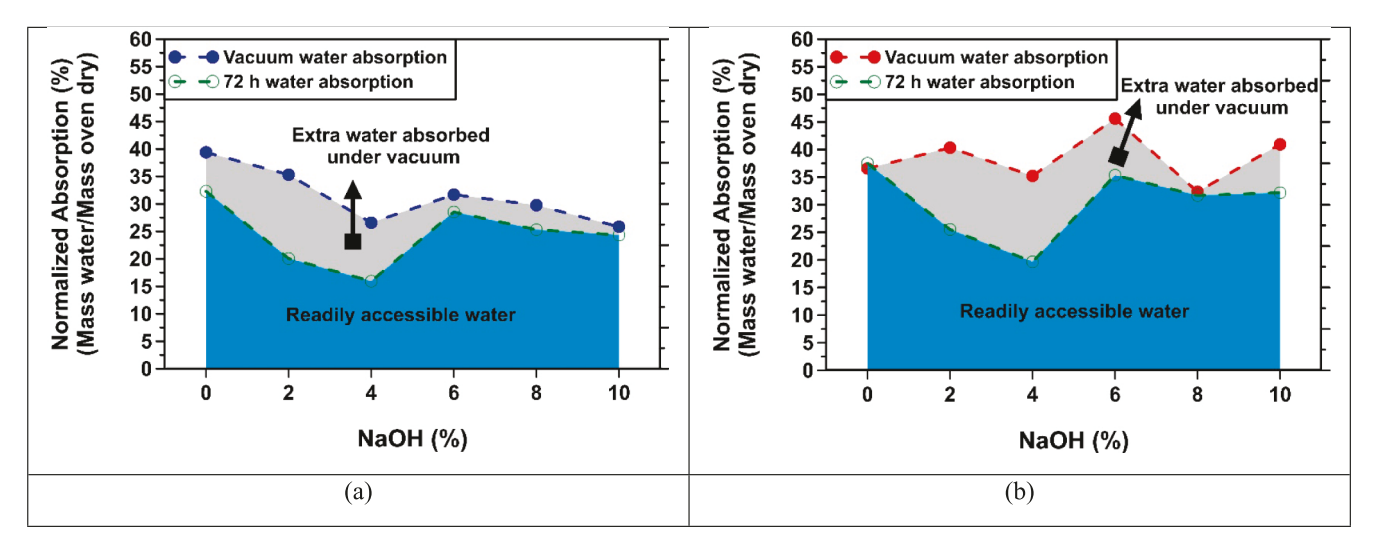


Fig. 9. Vacuum and 72 h water absorption for (a) F-FA LWA and (b) C-FA LWA; the blue area shows the water that is readily absorbed by the LWA during 72 h and is accessible for internal curing, while the gray area shows the extra water that can be absorbed by the LWA under vacuum. (For interpretation of the references to color in this figure legend, the reader is referred to the web version of this article.)

4.4. Porosity

Fig. 10 shows the porosity of the open or connected porosity of F-FA and C-FA LWA obtained using buoyancy and XCT techniques. The open porosity should follow the trend that was observed for vacuum absorption. This is because open porosity refers to the volume percentage of the pores that are capable of absorbing water as measured by vacuum absorption (see Fig. 7(a) and (b)).

As can be seen from Fig. 10(a), the buoyancy open porosity decreased for F-FA LWA as the NaOH concentration increased exhibiting a behavior similar to that of the vacuum absorption. In other words, the addition of NaOH to F-FA LWA led to an increase of closed pores. For C-FA LWA, the buoyancy open porosity values also showed the same trend as did the vacuum absorption, demonstrating the randomness of the pore structure during sintering. C-FA 6 % had the highest average open porosity, equal to 55.8 %.

The empty square symbols represent the open porosity obtained through XCT. It should be noted that XCT scanning produced a voxel size of about 19 μ m; therefore, any pores with size below that value were not distinguishable in segmentation, and thus were not reflected in the measured porosity. As a result, the porosity measured through XCT for

both F-FA and C-FA LWA had lower values than those obtained through the buoyancy method. The difference between the open porosity values obtained through these two methods indicates the porosity contribution from the pores smaller than 19 µm. Moreover, it should be noted that for the porosity obtained by XCT to be comparable with the buoyancy porosity, the XCT open porosity values are shown on Fig. 10. For this purpose, the closed porosity was calculated and deducted from the total porosity to obtain the open porosity through the XCT method. To obtain the closed porosity, first, in the segmented solid dataset the inner enclosed voxels (i.e., voxels associated with pore phase that are not finding any path to touch the VOI surface) were filled (added to the dataset) using the available function in the Dragonfly software. Next, the obtained dataset was subtracted from the segmented solid dataset to only obtain the closed pore volume. Finally, the volume of closed pores was divided by the VOI's volume to obtain the closed porosity. The maximum closed porosity measured by XCT for all the LWA was that of F-FA 2 %, which was equal to 1.1 %. For F-FA LWA, the general trend suggests that increasing the NaOH concentration increased the porosity obtained through XCT. This is opposite to the trend observed for total porosity measured through the buoyancy method. The XCT porosity trend implies the formation of larger pores (in the category of greater

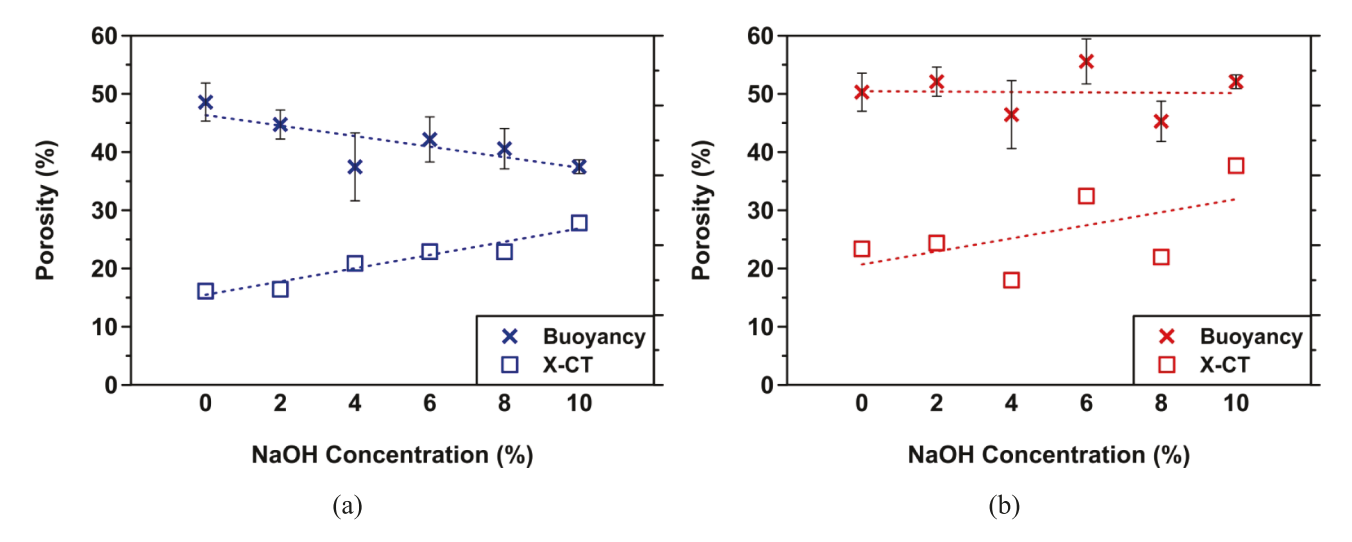


Fig. 10. The open porosity of (a) F-FA LWA and (b) C-FA LWA (the error bars indicate \pm one standard deviation for three replicates) based on buoyancy technique; the XCT porosity shows the open porosity (i.e., total porosity minus closed porosity both obtained using XCT) based upon single measurement.

than 19 μ m) in the LWA that were distinguishable by XCT. Interestingly, the measured XCT porosity for C-FA LWA followed the same point-by-point trend as the total open porosity obtained through the buoyancy method. At the same time, the general trend for the XCT porosity was to increase as the amount of NaOH increased. This could be related to the formation of larger pores that were distinguishable by the XCT method.

The difference between buoyancy and XCT porosity indicates that how the porosity as measured by XCT depends on the voxel size, since pores smaller than one voxel would not contribute to the XCT porosity. More discussion on the porosity in different pore categories is provided in Section 4.6.1.

4.5. Water desorption behavior

The water desorption behavior of a LWA is particularly important if the LWA is to be used for the internal curing of the concrete. The desorption isotherm can indicate how water is released from the LWA pore structure to the concrete matrix during the concrete selfdesiccation period. Fig. 11 shows the desorption isotherms for F-FA and C-FA LWA with 2 %, 6 %, and 10 % NaOH concentration. According to ASTM C1761, the LWA must release more than 85 % of its absorbed water at 94 % RH. For F-FA LWA (Fig. 11(a)), all the LWA released more than 92 % of their absorbed water at 94 % RH, in the following order: F-FA 10 % > F-FA 2 % > F-FA 6 %. The coarser the pore structure of LWA (in the range of less than 50 nm [41]), the easier it will be for the LWA to release the absorbed water as the RH decreases. This is because larger pores have lower capillary suction and so less ability to hold on to the absorbed water [41,42]. Accordingly, it appears that the F-FA 10 % had a coarser pore structure compared to F-FA 2 %, and F-FA 2 % had a coarser pore structure compared to F-FA 6 %. More discussion on the pore size distribution of the LWA is provided in Section 4.6.

All C-FA LWA (Fig. 11 (b)) released more than 98 % of their absorbed water as the RH fell below 94 %. The C-FA LWA had very similar desorption isotherms indicating that these LWA should have a similar pore structure in the range of less than 50 nm pore size. A general comparison between F-FA LWA and C-FA LWA suggests that C-FA LWA released more of its absorbed water than did F-FA LWA as the RH decreased. Accordingly, it can be inferred that C-FA LWA had a coarser pore structure compared to F-FA LWA.

4.6. Pore size distribution

To characterize the pore structure of the LWA, a combination of

Laplace equation can be used to obtain the distribution of pores smaller than 50 nm. Moreover, using this technique the normalized volume pores in the macropore region i.e., pores greater than 50 nm can be obtained. XCT was used to characterize the porosity and distribution of the pores greater than 19 μ m. In the following sections, first, using a combination of DVSA and XCT the porosity share distribution of the LWA is characterized. Next, using DVSA the pore size distribution in the range of pores smaller than 50 nm is discussed. Finally, using the XCT the pore size distribution of the LWA in the range of pores greater than 19 μ m is characterized.

DVSA and XCT was used. DVSA combined with the Kelvin-Young-

4.6.1. Porosity share distribution

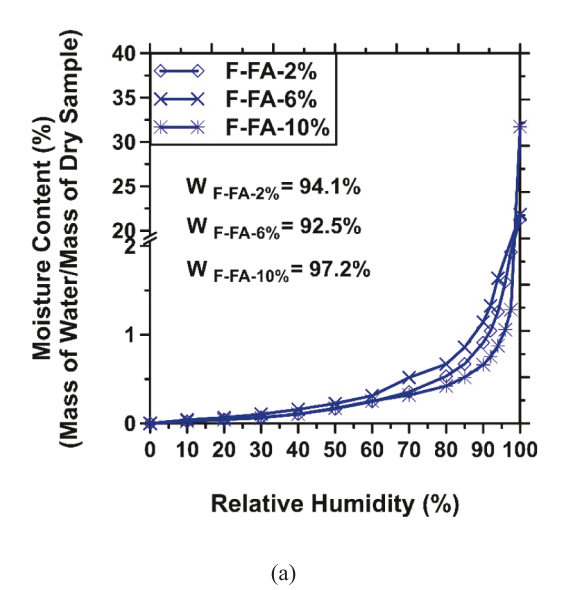
Fig. 12 shows the normalized porosity for three pore size categories: greater than 19 μm , between 19 μm and 50 nm, and less than 50 nm. In this case, "normalized" means that the sum of these three porosities equals 100 %. The normalized porosity of LWA in the range of pores smaller than 50 nm can be obtained according to Equation 5. The normalized porosity for the pores greater than 19 μm was obtained according to Equation 6. Finally, normalized porosity for the pores between 50 nm and 19 μm was obtained using Equation (7).

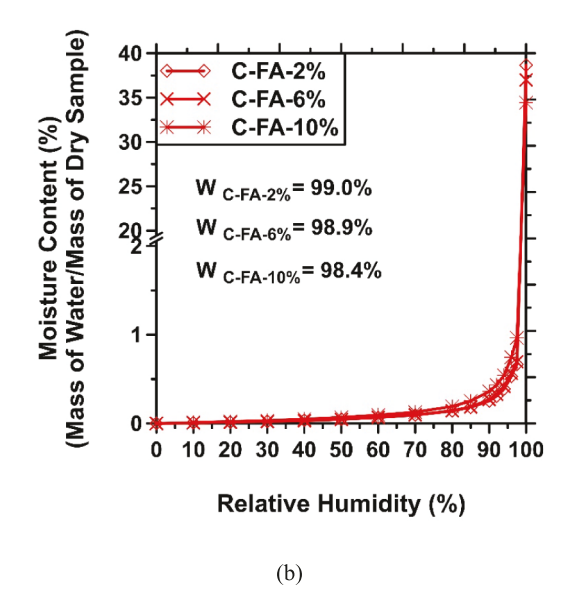
Normalized porosity_(<50 nm) =
$$\left(1 - \frac{Moisture\ content\ @97.5\%\ RH}{Moisture\ content\ @\ SSD}\right) *100\%$$
 (5)

Normalized porosity<sub>(>19
$$\mu m$$
)</sub> = $\frac{XCT \, porosity}{Bouyancy \, porosity} *100\%$ (6)

Normalized porosity<sub>(50nm< <19
$$\mu$$
m)</sub> = 100% – (Normalized porosity_(50 nm) + Normalized porosity_(>19 μ m)) (7)

As can be seen for F-FA LWA Fig. 12(a), the porosity originating from pores smaller than 50 nm constituted the smallest portion of the normalized total porosity. This porosity type was the largest for F-FA 6% and the smallest for F-FA 10% with 11.5% and 4% normalized porosity, respectively. As the NaOH concentration increased, the intermediate porosity share (i.e., the pores bigger than 50 nm and smaller than 19 μm) decreased, while the normalized porosity of the pores greater than 19 μm increased (macropore region). This observation demonstrated the effect of NaOH as the fluxing agent on the liquid phase formation and its viscosity and consequently the pore structure of the





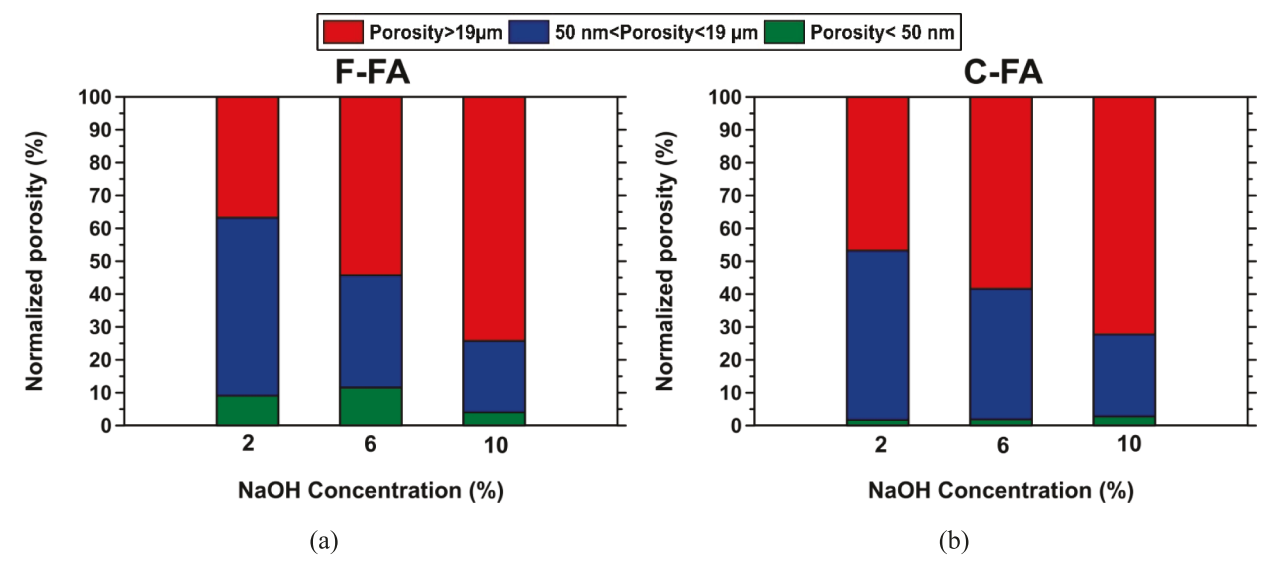


Fig. 12. The normalized porosity fraction in the range of greater than 19 µm, between 19 µm and 50 nm and less than 50 nm for (a) F-FA LWA and (b) C-FA LWA.

LWA. Indeed, the addition of higher NaOH concentration coarsened the pore structure of the LWA.

For all C-FA LWA (Fig. 12(b)), the porosity fraction of the pores smaller than 50 nm was even smaller than that of F-FA LWA and had a contribution of less than 3 % to the normalized total porosity. In other words, the majority (more than 97 %) of the pores belong to the macropore region (i.e., pores greater than 50 nm). This observation suggested that macropores in C-FA LWA were mostly responsible for the 72 h water absorption. The same trend as observed in F-FA LWA was seen for C-FA LWA for intermediate porosity and porosity originating from the pores greater than 19 μm .

4.6.2. Pore characterization through DVSA

The desorption isotherms obtained through DVSA (see Fig. 11) can be used to characterize the pore size distribution of a porous material based on the change in RH and desorbed water from the pores [43]. The Kelvin-Young-Laplace equation [44] correlates the pore radius to RH in a water-filled pore according to Equation 8, where γ is water surface tension, RH is relative humidity, V_m is molar mass, R is gas constant i.e.,

 $8.314 \text{ J.K}^{-1}.\text{mol}^{-1}$, and T is temperature (K).

$$r = \frac{2\gamma}{\ln(RH)} * \frac{V_m}{RT} \tag{8}$$

Fig. 13 shows the pore size distribution for F-FA and C-FA LWA. The pores are categorized in the range of gelpores (less than 5 nm), mesopores (between 5 nm and 50 nm) and macropores (greater than 50 nm). Fig. 13(a) shows that F-FA 6 % had the finest pore structure where 3 % of the pores were placed in the gelpore region, about 9 % of the pores were in the mesopore region, and more than 88 % of the pores were in the macropore region. F-FA 2 % had a slightly coarser pore structure compared to that of F-FA 6 %, where more than 91 % of the pore volume were in the macropore region. However, increasing the NaOH concentration to 10 % had a significant effect on the F-FA LWA pore structure. F-FA 10 % had the coarsest pore structure, where the distribution of the pores shifted from the gelpore and mesopore categories toward the macropore category. For F-FA 10 %, more than 96 % of the pores were placed in the macropore category, indicating that addition of high NaOH concentration promotes the formation of macropores, easing water

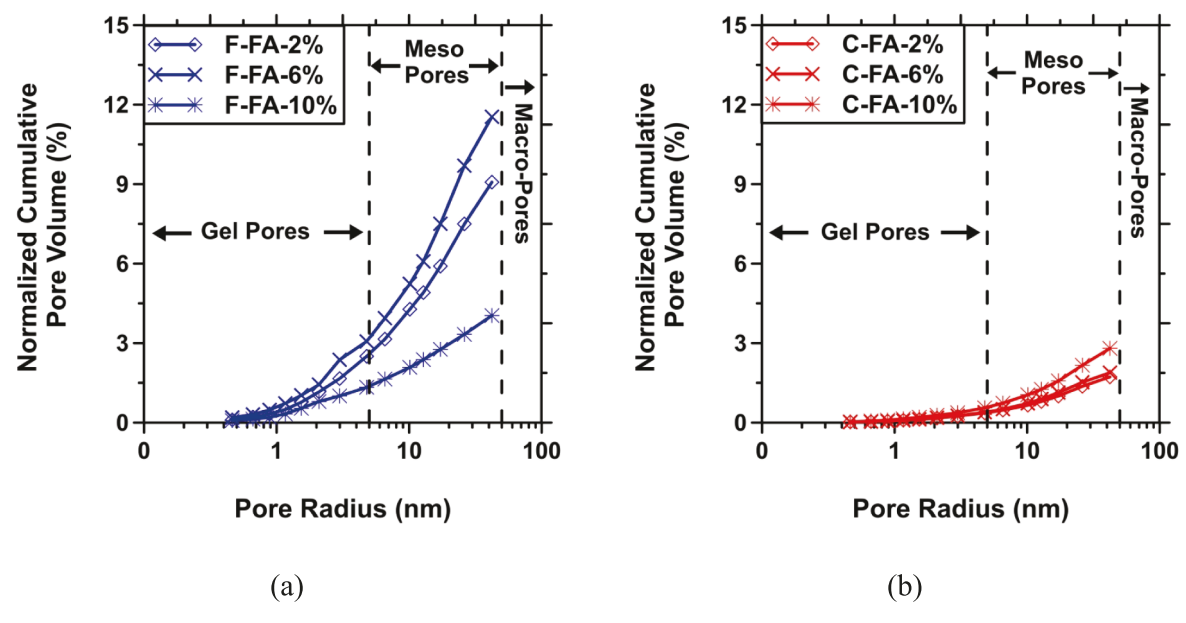


Fig. 13. The corresponding pore size distribution obtained from desorption isotherms for (a) F-FA LWA and (b) C-FA LWA.

release from the LWA.

The pore size distribution for the C-FA 2%, 6%, and 10%, shown in Fig. 13(b), indicated a very similar pore structure with different NaOH concentrations in the gelpores and mesopores regions. It appears that more than 97% of the pores are in the macropore region. The addition of NaOH to the C-FA LWA has a minimal impact on the pore structure in the gel and mesopore regions. This could be related to low viscosity of liquid phase in the C-FA LWA due to high CaO content that allowed easier expansion of the gas filled pores [16] during sintering and forming more larger pores [13]. As such, the majority of the pores (more than 97%) were macropores.

A comparison between F-FA and C-FA LWA suggests a finer pore structure for F-FA LWA. Balapour et al. [16] showed that a possible reason for the finer pore structure of F-FA LWA is related to the chemical composition of the F-FA material. The chemical composition of fly ash significantly affects the viscosity of the LWA during the sintering process. Since F-FA LWA had only 3.2 % CaO, higher viscosity values were obtained for the solid—liquid phase [13,14] in the LWA compared to C-FA LWA (which had 18.8 % CaO), leading to a smaller pore size formed during the sintering.

4.6.3. Pore characterization through XCT

Fig. 14(a) shows the pore size distribution for F-FA LWA obtained through XCT, with only pores with size greater than 19 µm measured. As can be seen from the cumulative distribution of the number of pores (see Fig. 14 (a)), d_{50} (i.e., the pore size below/above which 50 % of the pores by volume are smaller/larger) for F-FA 2 %, F-FA 6 %, and F-FA 10 % were 202 µm, 208 µm, and 218 µm, respectively. Based on the cumulative distribution of the pores for F-FA LWA, it can be inferred that increasing the NaOH concentration led to the development of larger pores in this LWA. This is mainly due to the formation of a higher amount of liquid phase with lower viscosity in the LWA during sintering that led to the formation of larger pores and coalescence of small pores to form larger pores [13,16]. Fig. 14(b) shows the cumulative normalized porosity fraction of different pore categories in F-FA LWA. D₅₀ shown on the figure is defined as the pore size at which cumulative normalized porosity reaches 50 %. For F-FA 2 %, F-FA 6 %, and F-FA 10 $\,$ %, the D_{50} was 500 $\mu m,\,534\,\mu m,$ and 714 $\mu m,$ respectively. The increase in D₅₀ with the increase in the NaOH concentration confirmed the formation of larger pores in the F-FA LWA.

As can be seen from Fig. 15(a), the d_{50} value for all the C-FA LWA samples was about 213 $\mu m.$ Based on the cumulative distribution of the pores, it can be observed that among the C-FA LWA samples, C-FA 2 % had a higher frequency of pores smaller than 300 μm in its pore structure

compared to C-FA 6 % and C-FA 10 %. On the other hand, C-FA 6 % and C-FA 10 % had a very comparable pore frequency distribution in their pore structure with some higher pore frequency for C-FA 6 % in the 500 μm to 600 μm pore size category. According to Fig. 15(b), the D_{50} for the C-FA 2 %, C-FA 6 %, and C-FA 10 %, were 745 μm , 614 μm , and 738 μm , respectively. In contrast to the F-FA LWA, where a clear trend between the NaOH concentration and the value of D_{50} was revealed, there was no clear trend between these two parameters for C-FA LWA. According to D_{50} obtained for C-FA LWA (Fig. 15(b)) C-FA 2 % and C-FA 10 % had larger pores forming their pore structure compared to C-FA 6 %.

Table 4 shows the calculated permeability coefficients for F-FA and C-FA LWA in \times , y, and z directions for the pores greater than 19 μ m. The permeability coefficient can be used as an indication of pore connectivity in the LWA and to understand the effect of NaOH concentration on the development of pore structure. For F-FA LWA, as the NaOH concentration increased, the permeability coefficients increased in all directions. This observation further indicates that higher NaOH concentrations led to the formation of larger pores that are highly connected, leading to a higher permeability coefficient. The average permeability (averaged over three directions) for F-FA 6 % was 533 % higher than that of F-FA 2 %, and the F-FA 10 % average permeability was 429 % higher than that of F-FA 6 %.

The same trend of permeability coefficient was observed for C-FA LWA. The average permeability for C-FA 6 % was 102 % higher than that of C-FA 2 %, and C-FA 10 % average permeability was 26 % higher than that of C-FA 6 %. The effect of NaOH on increasing the permeability coefficient for C-FA was less significant compared to that of F-FA. Comparing the permeability coefficients between F-FA LWA and C-FA LWA indicates that all C-FA LWA samples had a higher permeability coefficient compared to the comparable F-FA LWA. This observation may justify the higher water absorption results obtained (see Fig. 8) for C-FA LWA.

5. Summary and conclusions

This paper characterized the engineering properties and pore structure of spherical F-FA (low calcium FA) and C-FA (high calcium FA) LWA that were prepared through sintering using NaOH as the fluxing agent. The LWA were prepared following a thermodynamics-guided framework for LWA production [13,15]. Properties including specific gravity, vacuum and time-dependent water absorption, porosity, water desorption, pore size distribution, and permeability of the LWA were characterized.

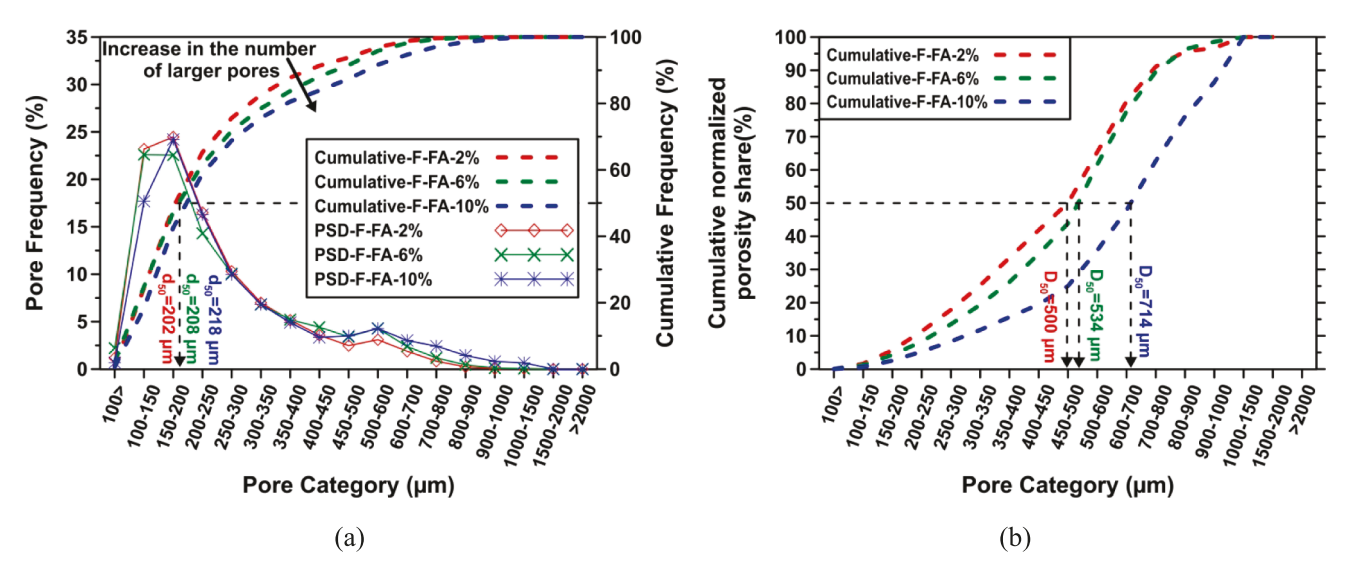


Fig. 14. F-FA LWA (a) pore size distribution and (b) normalized porosity share of pore categories obtained from XCT.

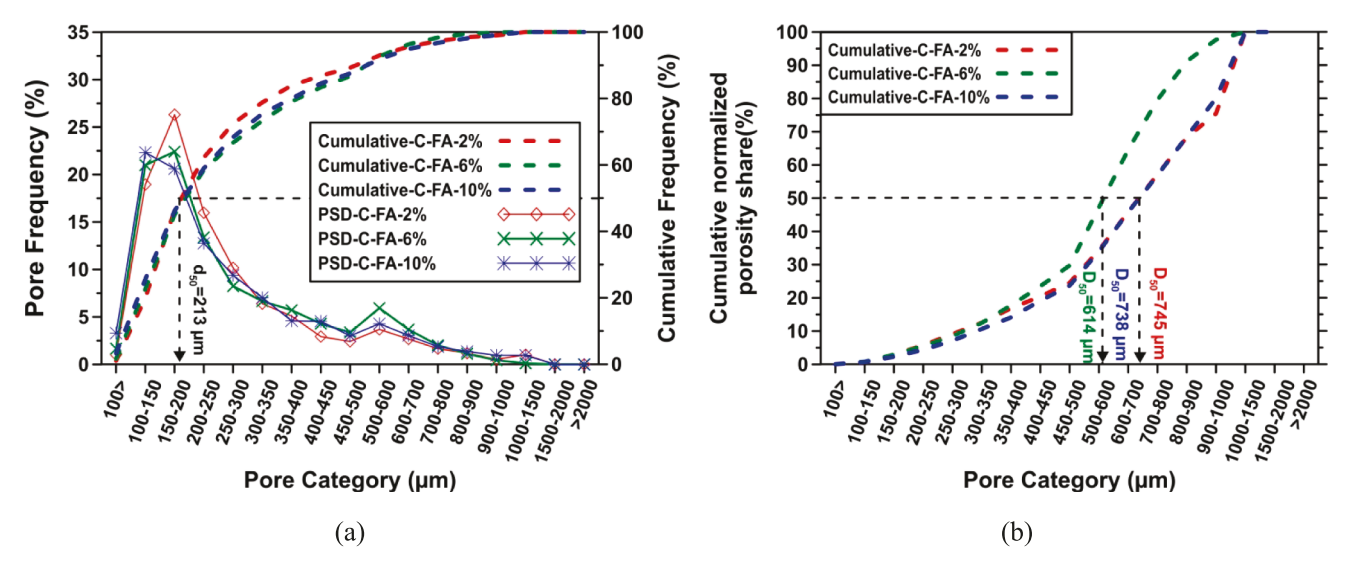


Fig. 15. C-FA LWA (a) pore size distribution and (b) normalized porosity share of pore categories obtained from XCT.

Table 4 The predicted permeability coefficient of F-FA and C-FA LWA in \times , y, and z directions obtained through XCT based upon single measurement.

Sample	Permeability Coefficient $(10^{-8} \times m^2)$				
	K _{xx}	K_{yy}	K_{zz}	Average in ×, y, and z directions	
F-FA 2 %	0.7	1.3	0.4	0.8	
F-FA 6 %	3.1	8.7	3.4	5.1	
F-FA 10 %	27.0	16.6	36.7	26.8	
C-FA 2 %	44.1	24.8	19.9	29.6	
C-FA 6 %	60.0	55.5	64.4	60.0	
C-FA 10 %	64.3	49.4	112.9	75.5	

- The specific gravity measurements demonstrated that the OD specific gravity for F-FA LWA ranged from 1.24 to 1.45 and C-FA from 1.22 to 1.41. Therefore, all the LWA were categorized as lightweight according to EN13055 due to having an OD specific gravity of less than
- The vacuum water absorption capacity showed that for F-FA LWA, vacuum absorption linearly decreased by 1.4 % per percentage of NaOH addition. However, the C-FA LWA vacuum absorption showed a variable trend as the NaOH increased. The linear and variable behavior for vacuum water absorption of F-FA and C-FA LWA could be attributed to the low and high calcium content in the fly ashes, respectively [13,16]. The 72 h water absorption for all the LWA was well above 5 % (the ASTM C1761 requirement for LWA to be used in concrete), showing great potential for these LWA to be used for concrete internal curing. The difference between the vacuum and 72 h water absorption showed that not all the open pores could be filled with water in 72 h. This observation can be related to the fact that some of the pores were filled with gas, which slowed down the capillary absorption of the LWA [38].
- The total open porosity obtained through the buoyancy method followed a trend similar to that of the vacuum water absorption for both F-FA and C-FA LWA. However, open porosity measured using XCT demonstrated an increasing trend as the NaOH concentration increased. Increase in the XCT porosity was due to the formation of larger pores in the LWA that became distinguishable by XCT, which only measured pores of size 19 µm or larger.
- The desorption isotherms showed that both F-FA and C-FA LWA released more than 85 % of their absorbed water at 94 % RH, which makes them suitable for concrete internal curing applications according to ASTM C1761. The DVSA method along with the Kelvin-Young-Laplace equation Indicated that for F-FA LWA, increasing

the NaOH concentration shifted the pores to the macropore region, which was due to formation of higher liquid phase content upon addition of higher NaOH concentration. For all C-FA LWA, more than 96 % of the pores fell in the macropore region, which indicated that mostly macropores are responsible for water absorption of the LWA.

- The LWA pore structure characterization indicated that the normalized porosity for F-FA LWA in the range of pores smaller than 50 nm ranged from 4 % to 11.5 %, while for C-FA LWA this normalized porosity ranged from 1.7 % to 2.8 %, suggesting a finer pore structure for F-FA LWA compared to C-FA LWA. The resulting finer structure for F-FA LWA in comparison with C-FA LWA could be related to higher solid–liquid phase viscosity that makes pore expansion and movement harder [13]. In addition, it was found that increasing the NaOH concentration for both types of LWA increased the normalized porosity in the range of pores greater than 19 μm.
- The pore size distribution obtained through XCT indicated that for F-FA LWA, the frequency of large pores increased as the NaOH concentration increased. The observed randomness in the pore structure of C-FA LWA may be attributed to the higher calcium content in the fly ash.
- The calculated permeability coefficient for both C-FA and F-FA LWA in three directions, using a pore-throat network derived from the XCT data, increased as the amount of NaOH increased, suggesting that the increase in pore connectivity allowed easier water movement in the LWA pore structure. However, LWA with low NaOH concentrations (0 % and 2 %) had high enough 72 h water absorption which implies the permeability was probably high enough to allow sufficient water penetration and absorption.

This study, along with the previous studies by the authors, suggests that a small concentration of NaOH (between 0 % and 2 %) might be used to produce FA-LWA with engineering properties desired for internal curing in concrete. Higher NaOH concentrations might result in improved engineering properties, but the environmental impact and cost associated with the use of NaOH might suggest using smaller doses of this fluxing agent. FA-LWA might be used for applications such as geotechnical filling, lightweight concrete production, and internal curing of concrete. As such, scaling up the production of spherical FA-LWA using a pelletizer (to produce spherical fresh pellets) and rotary furnace to bring the process closer to pilot-scale will be the focus of future studies [17]. In addition, if the FA-LWA is used in such applications the leachability of constituents of potential concern from the FA-LWA must be studied.

CRediT authorship contribution statement

Mohammad Balapour: Conceptualization, Formal analysis, Funding acquisition, Investigation, Methodology, Visualization, Writing – original draft, Writing – review & editing. Thiha Thway: Investigation. Newell Moser: Investigation, Writing – review & editing. Edward J. Garboczi: Investigation, Writing – review & editing. Y. Grace Hsuan: Writing – review & editing. Yaghoob Farnam: Funding acquisition, Project administration, Supervision, Writing – review & editing.

Declaration of Competing Interest

The authors declare that they have no known competing financial interests or personal relationships that could have appeared to influence the work reported in this paper.

Data availability

The authors do not have permission to share data.

Acknowledgments

This work was supported in part by the National Science Foundation under PFI–TT 1918838 grant and was performed at Drexel University in the Advanced and Sustainable Infrastructure Materials (ASIM) Lab. Any opinions, findings, and conclusions or recommendations expressed in this material are those of the authors and do not necessarily reflect the views of the National Science Foundation.

References

- [1] American Coal Ash Association, ACCA 2019 CCP Survey Results, (2019).
- [2] A.J. Bednar, D.E. Averett, J.M. Seiter, B. Lafferty, W.T. Jones, C.A. Hayes, M. A. Chappell, J.U. Clarke, J.A. Steevens, Characterization of metals released from coal fly ash during dredging at the Kingston ash recovery project, Chemosphere 92 (11) (2013) 1563–1570.
- [3] A.D. Lemly, Damage cost of the Dan River coal ash spill, Environ. Pollut. 197 (2015) 55-61.
- [4] Z.T. Yao, X.S. Ji, P.K. Sarker, J.H. Tang, L.Q. Ge, M.S. Xia, Y.Q. Xi, A comprehensive review on the applications of coal fly ash, Earth-Science Rev. 141 (2015) 105–121.
- [5] ASTM C618-19, Standard Specification for Coal Fly Ash and Raw or Calcined Natural Pozzolan for use in Concrete, West Conshohocken, PA, USA ASTM Int. (2019).
- [6] M. AASHTO, 295-19: Standard Specification for Coal Fly Ash and Raw or Calcined Natural Pozzolan for Use in Concrete, (2019).
- [7] S. Chandra, L. Berntsson, Lightweight Aggregate Concrete, Elsevier, 2002.
- [8] M. Balapour, R. Rao, S. Spatari, Y.G. Hsuan, Y. Farnam, Engineering Properties of Fly Ash-Based Lightweight Aggregate, in: World Coal Ash Conf. (WOCA), St. Louis, MO, May 13-16, 2019.
- [9] M. Dondi, P. Cappelletti, M. D'Amore, R. de Gennaro, S.F. Graziano, A. Langella, M. Raimondo, C. Zanelli, Lightweight aggregates from waste materials: reappraisal of expansion behavior and prediction schemes for bloating, Constr. Build. Mater. 127 (2016) 394–409, https://doi.org/10.1016/j.conbuildmat.2016.09.111.
- [10] P. Chindaprasirt, C. Jaturapitakkul, W. Chalee, U. Rattanasak, Comparative study on the characteristics of fly ash and bottom ash geopolymers, Waste Manag. 29 (2) (2009) 539–543.
- [11] M. Aineto, A. Acosta, J. Rincon, M. Romero, Thermal expansion of slag and fly ash from coal gasification in IGCC power plant, Fuel. 85 (16) (2006) 2352–2358.
- [12] J.M.J.M. Bijen, Manufacturing processes of artificial lightweight aggregates from fly ash, Int. J. Cem. Compos. Light. Concr. 8 (3) (1986) 191–199.
- [13] M. Balapour, R. Rao, E.J. Garboczi, S. Spatari, Y.G. Hsuan, P. Billen, Y. Farnam, Thermochemical principles of the production of lightweight aggregates from waste coal bottom ash, J. Am. Ceram. Soc. 104 (1) (2021) 613–634.
- [14] P. Billen, M. Mazzotti, L. Pandelaers, N. Ye oo, W. Zhao, Z. Liu, J. Redus, I. Diaz Loya, I. Bartoli, Y. Farnam, S. Spatari, Y.G. Hsuan, Melt ceramics from coal ash: Constitutive product design using thermal and flow properties, Resour. Conserv. Recycl. 132 (2018) 168–177.
- [15] M. Balapour, T. Thway, R. Rao, N. Moser, E.J. Garboczi, Y.G. Hsuan, Y. Farnam, A thermodynamics-guided framework to design lightweight aggregate from waste coal combustion fly ash, Resour. Conserv. Recycl. 178 (2022), 106050.

- [16] M. Balapour, W. Zhao, E.J. Garboczi, N.Y. Oo, S. Spatari, Y.G. Hsuan, P. Billen, Y. Farnam, Potential use of lightweight aggregate (LWA) produced from bottom coal ash for internal curing of concrete systems, Cem. Concr. Compos. 105 (2020), 103428.
- [17] M. Balapour, M.H. Khaneghahi, E.J. Garboczi, Y.G. Hsuan, D.E. Hun, Y. Farnam, Off-spec fly ash-based lightweight aggregate properties and their influence on the fresh, mechanical, and hydration properties of lightweight concrete: a comparative study, Constr. Build. Mater. 342 (2022) 128013.
- [18] D.P. Bentz, W.J. Weiss, Internal curing: a 2010 state-of-the-art review, US Department of Commerce, National Institute of Standards and Technology ..., 2011.
- [19] H.S. Esmaeeli, Y. Farnam, D.P. Bentz, P.D. Zavattieri, W.J. Weiss, Numerical simulation of the freeze-thaw behavior of mortar containing deicing salt solution, Mater. Struct. 50 (2017) 96, https://doi.org/10.1617/s11527-016-0964-8.
- [20] K. Scrivener, R. Snellings, B. Lothenbach, A Practical Guide to Microstructural Analysis of Cementitious Materials, CRC Press, 2018.
- [21] ASTM Subcommittee C09.20, C0127 Standard Test Method for Relative Density (Specific Gravity) and Absorption of Coarse Aggregate, ASTM Int. (2015) 5. https://doi.org/10.1520/C0127-15.2.
- [22] Dragonfly, (2018). https://www.theobjects.com/dragonfly/index.html.
- [23] Y. Shields, E. Garboczi, J. Weiss, Y. Farnam, Freeze-thaw crack determination in cementitious materials using 3D X-ray computed tomography and acoustic emission, Cem. Concr. Compos. 89 (2018) 120–129.
- [24] C.H. Li, C.K. Lee, Minimum cross entropy thresholding, Pattern Recognit. 26 (4) (1993) 617–625.
- [25] F.H. Kim, S.P. Moylan, E.J. Garboczi, J.A. Slotwinski, Investigation of pore structure in cobalt chrome additively manufactured parts using X-ray computed tomography and three-dimensional image analysis, Addit. Manuf. 17 (2017) 23–38.
- [26] N. Dhanachandra, K. Manglem, Y.J. Chanu, Image segmentation using K-means clustering algorithm and subtractive clustering algorithm, Procedia Comput. Sci. 54 (2015) 764–771.
- [27] K. Lyu, E.J. Garboczi, W. She, C. Miao, The effect of rough vs. smooth aggregate surfaces on the characteristics of the interfacial transition zone, Cem. Concr. Compos. 99 (2019) 49–61.
- [28] R. Moini, A. Baghaie, F.B. Rodriguez, P.D. Zavattieri, J.P. Youngblood, J. Olek, Quantitative microstructural investigation of 3D-printed and cast cement pastes using micro-computed tomography and image analysis, Cem. Concr. Res. 147 (2021), 106493.
- [29] D. Arthur, S. Vassilvitskii, k-means++: The advantages of careful seeding, Stanford, 2006.
- [30] N. Saxena, R. Hofmann, F.O. Alpak, J. Dietderich, S. Hunter, R.J. Day-Stirrat, Effect of image segmentation & voxel size on micro-CT computed effective transport & elastic properties, Mar. Pet. Geol. 86 (2017) 972–990.
- [31] R.D. Hanna, R.A. Ketcham, X-ray computed tomography of planetary materials: a primer and review of recent studies, Chemie Der Erde-Geochem. 77 (4) (2017) 547–572.
- [32] A. Putz, J. Hinebaugh, M. Aghighi, H. Day, A. Bazylak, J.T. Gostick, Introducing OpenPNM: an open source pore network modeling software package, ECS Trans. 58 (2013) 79.
- [33] J.T. Gostick, Versatile and efficient pore network extraction method using marker-based watershed segmentation, Phys. Rev. E. 96 (2017) 23307.
- [34] Z.A. Khan, T. Tranter, M. Agnaou, A. Elkamel, J. Gostick, Dual network extraction algorithm to investigate multiple transport processes in porous materials: Imagebased modeling of pore and grain scale processes, Comput. Chem. Eng. 123 (2019) 64–77
- [35] L.E. Beckingham, C.A. Peters, W. Um, K.W. Jones, W.B. Lindquist, 2D and 3D imaging resolution trade-offs in quantifying pore throats for prediction of permeability, Adv. Water Resour. 62 (2013) 1–12.
- [36] C.-L. Hwang, V.-A. Tran, A study of the properties of foamed lightweight aggregate for self-consolidating concrete, Constr. Build. Mater. 87 (2015) 78–85.
- [37] A. Standard, Standard Specification for Lightweight Aggregate for Internal Curing of Concrete, Annu. B. ASTM Stand. ASTM Int. West Conshohocken, PA. (2013).
- [38] L.E. Dalton, K. Jarvis, M. Pour-Ghaz, The effect of gas solubility on the secondary sorption in a Portland cement mortar observed by X-ray CT, Transp. Porous Media. 133 (3) (2020) 397–411.
- [39] Y. Ren, Q. Ren, Z. Huo, X. Wu, J. Zheng, O. Hai, Preparation of glass shell fly ashclay based lightweight aggregate with low water absorption by using sodium carbonate solution as binder, Mater. Chem. Phys. 256 (2020), 123606.
- [40] M. Balapour, Characterizing Physical Properties of Lightweight Aggregate Made from Waste Coal Ash Using X-Ray Computed Tomography, (2020).
- [41] H.S. Esmaeeli, Y. Farnam, J.E. Haddock, P.D. Zavattieri, W.J. Weiss, Numerical analysis of the freeze-thaw performance of cementitious composites that contain phase change material (PCM), Mater. Des. 145 (2018) 74–87.
- [42] T.A. Holm, O.S. Ooi, T.W. Bremner, Moisture dynamics in lightweight aggregate and concrete, in: Theodore Bremner Symp. High-Performance Light. Concr., 2003: pp. 167–184.
- [43] C. Hall, W.D. Hoff, Water transport in brick, stone and concrete, (2002).
- [44] F. Althoey, Y. Farnam, Performance of calcium aluminate cementitious materials in the presence of sodium chloride, J. Mater. Civ. Eng. 32 (2020) 4020277.